Nonlinear Dyn (2018) 92:1619–1635
https://doi.org/10.1007/s11071-018-4150-0

ORIGINAL PAPER

On decoupling trajectory tracking control of unmanned powered parafoil using ADRC-based coupling analysis and dynamic feedforward compensation

Shuzhen Luo · Qinglin Sun · Mingwei Sun · Panlong Tan · Wannan Wu · Hao Sun · Zengqiang Chen

Received: 7 September 2017 / Accepted: 14 February 2018 / Published online: 20 February 2018

Abstract Powered parafoil system is strongly nonlinear and contains complicated cross-coupling characteristic. Under the variable wind disturbance, more severe cross-couplings are generated due to the frequent operation of control quantities, probably resulting in large deviations or instability in the control process. To tackle this problem, a novel decoupling control approach using active disturbance rejection control (ADRC)-based feedforward coupling compensation is proposed. First, the dynamic cross-coupling relations are analyzed and designed as the known disturbance of extended state observer (ESO) to be compensated in the improved control law, so that the estimation ability of ESO is enhanced. Moreover, under the feedforward cross-coupling compensation, this complex nonlinear powered parafoil system is constructed as two decoupled integrators which can be easily controlled, while all other model uncertainties and external disturbance are treated as the unknown disturbance of ESO to be estimated and canceled, such that the tracking precision and disturbance rejection capacity are improved simultaneously. Eventually, mathematical simulations, robustness performance, and experimental results demonstrate that the proposed decoupling control approach has better tracking performance and robustness against the internal and external disturbances compared with the conventional ADRC and PID.

Keywords Dynamic coupling · Powered parafoil · Decoupling trajectory tracking control · Feedforward coupling compensation · Extended state observer

S. Luo · Q. Sun (✉) · M. Sun · W. Wu · H. Sun · Z. Chen
Department of Computer and Control Engineering, Nankai University, Tianjin, China
e-mail: sunql@nankai.edu.cn

P. Tan
Department of Electrical Engineering and Energy, Tianjin Sino-German University of Applied Sciences, Tianjin, China

1 Introduction

Powered parafoil, as a new kind of flexible wing vehicle, is composed of a parafoil and a payload equipped with a motor or propeller. It retains the flight characteristics of the traditional parafoil: gliding motion without maneuvering, turning motion through pulling a single steering line, and soft landing through pulling the left and right steering lines on the trailing edge of canopy symmetrically. Compared with traditional parafoil, the powered parafoil has much farther flight distances, and the longitudinal vertical velocity can be controlled, which can maintain the flight at a constant height, even to climb. By virtue of these flight properties, the powered parafoil extends possible applications of traditional parafoil in both military and civil fields, such as military reconnaissance, demisting at the airport and harbor, and advertising [1–5].

Powered parafoil system has strong nonlinearity and is highly susceptible to atmospheric wind disturbance

due to low flight speed and the flexible fabric materials of the canopy [6–9]. Moreover, this system is strongly cross-coupled and contains complicated nonlinear dynamics. The actuators for powered parafoil involve lateral brake deflection by pulling left or right steering lines on the trailing edge of canopy and longitudinal thrust provided by the propeller. Here the former one mainly controls the flight direction, and the latter controls the altitude. However, these two actuators have cross-coupling effects. Longitudinal thrust not only has a significant impact on the vertical velocity, but also produces the nonlinear coupling effect on lateral turning motion; lateral brake deflection affects the turning radius as well as longitudinal altitude. More importantly, the variable wind disturbance will lead to more serious cross-couplings [1,10]. Therefore, accurate trajectory tracking control with high capacity of resisting couplings and disturbance of powered parafoil system still remains a challenging problem.

The existing studies focused mostly on a single lateral trajectory tracking or longitudinal control, and the investigations on the cross-coupling relations between the longitudinal and lateral motion were rarely carried out. Slegers and Costello [11] proposed a model predictive control strategy for lateral heading control of a parafoil and payload aircraft. Aoustin and Martynenko [12] designed a nonlinear control law based on the partial feedback linearization just for controlling the longitudinal motion. Ochi et al. [13] employed a three-term PID controller including the asymmetric brake deflection, symmetric brake, and thrust. Li et al. [14] also utilized a three-term PID controller, where an energy function considering the altitude and forward velocity was added, but the longitudinal control of altitude was independently designed. Since the powered parafoil system suffers from the variable wind disturbance substantially, a trajectory tracking controller based on ADRC was constructed to improve the anti-disturbance ability [15–17]. Through regarding the cross-couplings, model uncertainties and external disturbance as total disturbances, the total disturbances were estimated via the extended state observer (ESO) using input and output information, and compensated by real-time dynamic feedback in ADRC. Moreover, the ESO goes beyond a traditional disturbance observer (DOB) like DOB [18–20], because not only the external, but also the internal disturbances are estimated [21–28]. However, for the powered parafoil system, these disturbances such as model uncertainties, nonlinear cross-coupling influences, and variable external disturbance are all estimated by ESO, which will cause the considerable oscillation and inaccurate estimation under the variable wind environment, resulting in the limitation of the controller to achieve satisfactory performance. Moreover, the cross-couplings become more severe under the actual variable wind environment, probably leading to large deviations and instability in the control process. This problem highlights the motivation for this study. If the cross-couplings can be compensated directly, the suppression of the disturbance and tracking precision of the control system will be improved simultaneously by improving the estimation ability of ESO.

In this paper, different from the existing controllers, a novel decoupling control approach using ADRC-based feedforward coupling compensation (abbreviation, DADRC) is proposed. The nonlinear coupling relations are firstly solved and designed as the known disturbance of ESO to enhance the estimation ability of ESO. Moreover, the cross-couplings are compensated in the improved control law. Furthermore, under the couplings feedforward compensation, this complex powered parafoil system is constructed as two decoupled integrators which can be easily controlled, while all other model uncertainties and external disturbance are treated as the unknown disturbance of ESO to be estimated and canceled. The remainder of the paper is organized as follows. The powered parafoil model is given in Sect. 2 as a basis for controller design and robust stability analysis. The cross-coupling relations between the lateral and longitudinal motion are analyzed and solved in Sect. 3. The proposed DADRC solution is presented in Sect. 4, followed by the simulations, robustness analysis, and experimental results in Sects. 5 and 6, respectively. Eventually, the conclusions are drawn in Sect. 7. The stability analysis of DADRC is also given in "Appendix".

2 System modeling

Compared with unpowered parafoil, the relative motion between the parafoil and payload should be taken into account, since they affect the payload attitude and the thrust direction. Considering the apparent mass and the relative motions, the model of the powered parafoil system involves eight dof, including three inertial position components of parafoil mass center, three Euler orientation angles of parafoil, and the relative pitch and yaw

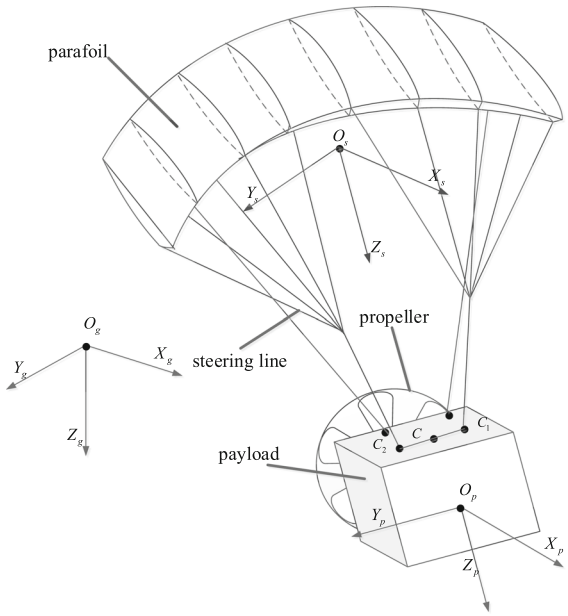

Fig. 1 Schematic of powered parafoil and related coordinate frames

motion between the parafoil and the payload. The following part of this section will briefly deduce the eight dof model of powered parafoil, and a more detailed derivation process can be found in [1,9]. A schematic of powered parafoil and related coordinate frames is shown in Fig. 1. Three main coordinate frames to be used are established: geodetic coordinate $O_{\mathrm{g}}x_{\mathrm{g}}y_{\mathrm{g}}z_{\mathrm{g}}$, parafoil body coordinate $O_{\mathrm{s}}x_{\mathrm{s}}y_{\mathrm{s}}z_{\mathrm{s}}$, and the payload coordinate $O_{\mathrm{p}}x_{\mathrm{p}}y_{\mathrm{p}}z_{\mathrm{p}}$.

In order to facilitate analysis, some reasonable hypotheses [1,4,9] are made as follows:

1. After the parafoil has been completely inflated, its aerodynamic configuration is steady without maneuver.
2. The mass center of the parafoil coincides with the aerodynamic pressure center.
3. The lift force of the payload is neglected; only its aerodynamic drag force is considered.

2.1 Motion equations of parafoil

The forces acting on the parafoil are the aerodynamic force $F_{\mathrm{s}}^{\mathrm{aero}}$, the gravity $F_{\mathrm{s}}^{\mathrm{G}}$, and the tension of lines $F_{\mathrm{s}}^{\mathrm{t}}$. Based on the theorem of momentum, these forces satisfy:

$$\frac{\partial P_{\mathrm{s}}}{\partial t} + W_{\mathrm{s}} \times P_{\mathrm{s}} = F_{\mathrm{s}}^{\mathrm{aero}} + F_{\mathrm{s}}^{\mathrm{G}} + F_{\mathrm{s}}^{\mathrm{t}} \tag{1}$$

$$\frac{\partial H_{\mathrm{s}}}{\partial t} + W_{\mathrm{s}} \times H_{\mathrm{s}} + V_{\mathrm{s}} \times P_{\mathrm{s}} = M_{\mathrm{s}}^{\mathrm{aero}} + M_{\mathrm{s}}^{f} + M_{\mathrm{s}}^{\mathrm{G}} + M_{\mathrm{s}}^{\mathrm{t}} \tag{2}$$

where the subscript s denotes the parafoil body coordinate; F and M denote the force and moment acting on the parafoil, respectively; the momentum and angular momentum of parafoil are represented as P_{s} and H_{s}, respectively; $V_{\mathrm{s}} = [u_{\mathrm{s}}, v_{\mathrm{s}}, w_{\mathrm{s}}]^{\mathrm{T}}$, $W_{\mathrm{s}} = [p_{\mathrm{s}}, q_{\mathrm{s}}, r_{\mathrm{s}}]^{\mathrm{T}}$ are defined as velocity and angular velocity of the parafoil, respectively. The aerodynamic force has been one of the key issues when modeling parafoil systems, and the lateral control is produced by changing the length of steering lines connected to outboard side and rear of the canopy. Pulling down steering lines leads to complex changes in the shape and orientation of the lifting surface; the downward bending of the trailing edge forms the brake deflection angle (the lateral control input). The change in the brake deflection angle will affect the aerodynamic force, and the relationship between the brake deflection and the aerodynamic force is given in Sect. 3.

Taking into account the apparent mass of the powered parafoil, P_{s} and H_{s} are given as:

$$\begin{bmatrix} P_{\mathrm{s}} \\ H_{\mathrm{s}} \end{bmatrix} = \begin{bmatrix} A_{\mathrm{a,O}} + A_{\mathrm{r,O}} \end{bmatrix} \begin{bmatrix} V_{\mathrm{s}} \\ W_{\mathrm{s}} \end{bmatrix} = \begin{bmatrix} A_1 & A_2 \\ A_3 & A_4 \end{bmatrix} \begin{bmatrix} V_{\mathrm{s}} \\ W_{\mathrm{s}} \end{bmatrix} \tag{3}$$

where $A_{\mathrm{r,o}}$ and $A_{\mathrm{a,o}}$ denote the real mass of parafoil and the apparent mass, respectively; $A_i (i = 1, \ldots, 4)$ denotes the third-order submatrix of $(A_{\mathrm{a,o}} + A_{\mathrm{r,o}})$.

2.2 Motion equations of payload

The forces acting on the payload are the aerodynamic force $F_{\mathrm{p}}^{\mathrm{aero}}$, the gravity $F_{\mathrm{p}}^{\mathrm{G}}$, the tension $F_{\mathrm{p}}^{\mathrm{t}}$, and the thrust $F_{\mathrm{p}}^{\mathrm{th}}$ produced by the propeller. The thrust $F_{\mathrm{p}}^{\mathrm{th}}$ is the longitudinal control quantity, and it can control the vertical velocity of the powered parafoil system by changing the pitch angle of the payload and the aerodynamic force. Since the gravity and thrust are assumed to act upon the mass center of the payload, the angular momentums due to gravity and thrust are ignored. The motion equations of the payload are presented as follows.

$$\frac{\partial P_{\mathrm{p}}}{\partial t} + W_{\mathrm{p}} \times P_{\mathrm{p}} = F_{\mathrm{p}}^{\mathrm{aero}} + F_{\mathrm{p}}^{\mathrm{t}} + F_{\mathrm{p}}^{\mathrm{G}} + F_{\mathrm{p}}^{\mathrm{th}} \tag{4}$$

$$\frac{\partial H_{\mathrm{p}}}{\partial t} + W_{\mathrm{p}} \times H_{\mathrm{p}} = M_{\mathrm{p}}^{\mathrm{aero}} + M_{\mathrm{p}}^{f} + M_{\mathrm{p}}^{\mathrm{t}} \tag{5}$$

where the subscript p denotes the payload coordinate; V_{p}, W_{p} are defined as velocity and angular velocity of the mass center of the payload, respectively; f denotes the friction; the momentum P_{p} and angular momentum H_{p} of the payload can be obtained by:

$$P_{\mathrm{p}} = m_{\mathrm{p}} V_{\mathrm{p}},\ H_{\mathrm{p}} = J_{\mathrm{p}} W_{\mathrm{p}} \tag{6}$$

where m_{p} denotes the mass of payload and J_{p} denotes its matrix form of the moment of inertial.

2.3 Constraint of velocity and angular velocity

The velocity and angular velocity between the parafoil and the payload are not independent of each other. The middle point c of two steering lines hanging on the payload is treated as the total connection point between the parafoil and payload. The kinematical constraint at point c is obtained by:

$$V_{\mathrm{p}} + W_{\mathrm{p}} \times L_{O_{\mathrm{p}}-c} = V_{\mathrm{s}} + W_{\mathrm{s}} \times L_{O_{\mathrm{s}}-c} \tag{7}$$

with the distance from the parafoil centroid and the payload centroid to the point c being $L_{O_{\mathrm{p}}-c}$ and $L_{O_{\mathrm{s}}-c}$, respectively. The relative motion between the parafoil and payload satisfies the angular velocity constraint:

$$W_{\mathrm{p}} = W_{\mathrm{s}} + \tau_{\mathrm{s}} + k_{\mathrm{p}} \tag{8}$$

where φ_{r} and θ_{r} denote the relative yaw angle and pitch angle, respectively. And $\tau_{\mathrm{s}} = [0, 0, \dot{\varphi}_{\mathrm{r}}]$ is represented in the parafoil coordinate, and $k_{\mathrm{p}} = [0, \dot{\theta}_{\mathrm{r}}, 0]$ is represented in the payload coordinate. Differentiating (7) yields:

$$\begin{aligned} &T_{\mathrm{p-s}} \dot{W}_{\mathrm{p}} - \dot{W}_{\mathrm{s}} - \dot{\tau}_{\mathrm{s}} - T_{p-s} \dot{\kappa}_{\mathrm{p}} \\ &\quad = W_{\mathrm{s}}^{\times} T_{\mathrm{p-s}} W_{\mathrm{p}} + \tau_{\mathrm{s}}^{\times} T_{\mathrm{p-s}} \kappa_{\mathrm{p}} \end{aligned} \tag{9}$$

where $T_{\mathrm{p-s}}$ is the transformation from payload coordinate to parafoil coordinate. Since the suspension line forms the connection between the parafoil and payload, on the basis of reciprocity of force, $F_{\mathrm{s}}^{\mathrm{t}}$ and $F_{\mathrm{p}}^{\mathrm{t}}$ satisfy:

$$F_{\mathrm{s}}^{\mathrm{t}} = -T_{\mathrm{p-s}} F_{\mathrm{p}}^{\mathrm{t}} \tag{10}$$

Based on aforementioned formulas, the state of the powered parafoil system $x = [V_{\mathrm{p}}, W_{\mathrm{p}}, V_{\mathrm{s}}, W_{\mathrm{s}}, \dot{\varphi}_{\mathrm{r}}, \dot{\theta}_{\mathrm{r}}]^{\mathrm{T}}$ is constructed, and the eight dof model of the powered parafoil system can be well built.

$$\dot{x} = \left(\left[D_1{}^{\mathrm{T}} D_2{}^{\mathrm{T}} D_3{}^{\mathrm{T}} D_4{}^{\mathrm{T}}\right]\right)^{-1} \left[E_1{}^{\mathrm{T}} E_2{}^{\mathrm{T}} E_3{}^{\mathrm{T}} E_4{}^{\mathrm{T}}\right] \tag{11}$$

where $D_1 - E_4$ are matrices from above formulas.

3 Dynamic coupling analysis between lateral and longitudinal motion

The control inputs for powered parafoils involve lateral brake deflection by pulling left or right steering lines on the trailing edge of canopy and longitudinal thrust provided by the propeller. Here the former one mainly controls the yaw angle, and the latter controls the longitudinal altitude. However, these two actuators have cross-coupling effects. In this section, the more detailed analysis about the cross-coupling relations between the lateral and longitudinal motions is given in this section.

3.1 Coupling influences between lateral and longitudinal motion

In this section, the cross-coupling influences between the lateral and longitudinal motions are analyzed through the simulation. Figure 2 illuminates the coupling influence between lateral and longitudinal motion. First, the left lateral brake deflection control is fixed with 20% at 40 s, and longitudinal thrust varies from 100 to 200 N at 60 s.

The powered parafoil system will produce a left turning motion under the left lateral brake deflection, and the turning radius decreases with the increase in the brake deflection. From Fig. 2a, when the longitudinal thrust is given by 100 N, the lateral motion produces a circle trajectory with a radius of 150 m, and with the increase in thrust from 100 to 200 N, the lateral turning radius decreased 20 and 35 m. Therefore, the larger the longitudinal thrust quantity, the smaller the lateral turn radius, and the nonlinear coupling influence becomes more evident as the thrust increases.

Next, the coupling influence of lateral brake deflection on the longitudinal motion is also analyzed. The

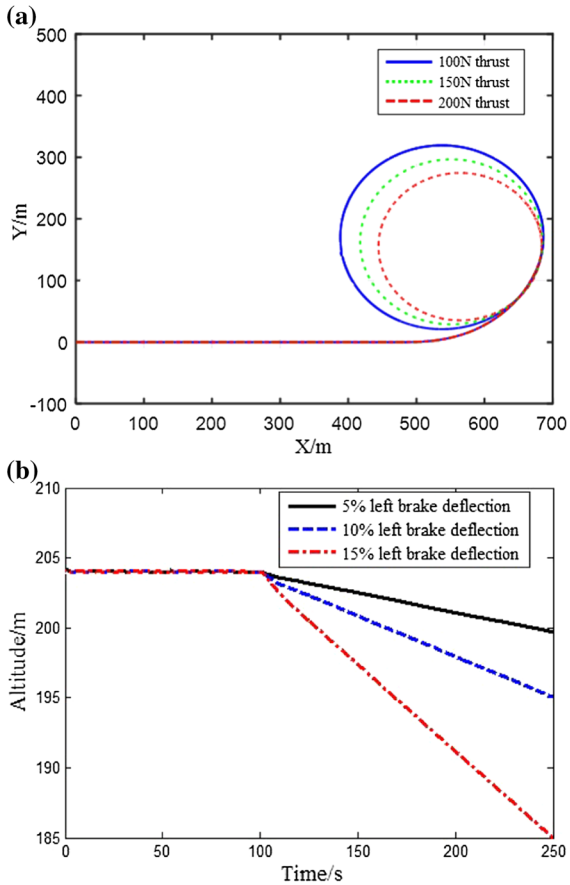

Fig. 2 Coupling influence between the lateral and longitudinal motion. **a** Coupling influence of longitudinal thrust on lateral turn radius. **b** Coupling influence of lateral brake deflection on longitudinal altitude

powered parafoil system can fly at a constant altitude under a certain longitudinal thrust. In this simulation, longitudinal thrust is set to maintain a constant altitude, the lateral brake deflection is gradually increased from 5 to 15% at 100 s, and the coupling influence of lateral brake deflection on the longitudinal altitude is shown in Fig. 2b. From Fig. 2b, the altitude declines with the increase in the brake deflection, and with the continuous increase in brake deflection, the altitude reduced intensely. When the lateral brake deflection is given by 5%, the longitudinal altitude decreased 4m, and with the increase in lateral brake deflection from 5 to 15%, the longitudinal altitude decreased 9 and 19 m. It is clearly shown that the longitudinal altitude of powered parafoil system is also affected by the lateral brake deflection. From aforementioned illuminations, the coupling influence of longitudinal thrust on lateral turning radius is more severe than the other. Under the constant lateral brake deflection, a great thrust quantity acting on the system will result in instability and even a stall phenomenon. Therefore, these nonlinear coupling effects between the lateral and longitudinal dynamics affect the tracking precision and stability of the control system.

3.2 Coupling of longitudinal thrust on lateral yaw angular acceleration

In this section, the coupling relation of longitudinal thrust on the lateral yaw angular acceleration is solved. From Fig. 1, the transformation of angular velocity between the geodetic coordinate and the parafoil coordinate is obtained by:

$$\begin{bmatrix} \dot{\zeta} \\ \dot{\theta} \\ \dot{\varphi} \end{bmatrix} = \begin{bmatrix} 1 & \sin\zeta\tan\theta & \cos\zeta\tan\theta \\ 0 & \cos\zeta & -\sin\zeta \\ 0 & \sin\zeta/\cos\theta & \cos\zeta/\cos\theta \end{bmatrix} \begin{bmatrix} p_s \\ q_s \\ r_s \end{bmatrix} \tag{12}$$

where $[\zeta, \theta, \varphi]^T$ denotes the roll angle, pitch angle, and yaw angle, respectively. Then, the yaw rate is obtained by:

$$\dot{\varphi} = q_s \sin\zeta/\cos\theta + r_s \cos\zeta/\cos\theta \tag{13}$$

Then, the yaw angular acceleration is yielded:

$$\begin{aligned} \ddot{\varphi} = {} & r_s \left(\frac{2\cos 2\zeta \sin\theta}{\cos^2\theta} q_s - \frac{\sin\zeta}{\cos\theta} p_s \right) + \dot{q}_s \left(\frac{\sin\zeta}{\cos\theta} \right) \\ & - {r_s}^2 \left(\frac{\sin 2\zeta \sin\theta}{\cos^2\theta} \right) + p_s q_s \left(\frac{\cos\zeta}{\cos\theta} \right) \\ & + {q_s}^2 \frac{\sin 2\theta \sin\zeta}{\cos^2\theta} + \dot{r}_s \left(\frac{\cos\zeta}{\cos\theta} \right) \end{aligned} \tag{14}$$

From (14), the relationship between the angular velocity components and the longitudinal thrust should be required. From (1), (4), and (10), the thrust is yielded as:

$$\begin{aligned} F_p^{th} = {} & m_p W_p{}^{\times} V_p + W_p m_p V_p - T_{p-s}{}^{-1} F_s^{aero} \\ & + T_{p-s}{}^{-1} W_s{}^{\times} (A_1 V_s + A_2 W_s) - T_{p-s}{}^{-1} F_s^{G} \\ & - F_p^{G} - F_p^{aero} + T_{p-s}{}^{-1} A_1 W_s{}^{\times} V_s \\ & + T_{p-s}{}^{-1} W_s{}^{\times} A_2 W_s \end{aligned} \tag{15}$$

Since the relationship between angular velocity components and the longitudinal thrust is required, the thrust is rewritten as follows with the variable F_{d} being irrelevant terms from (15).

$$\begin{aligned} {F_{\mathrm{p}}}^{\mathrm{th}} &= {T_{\mathrm{p-s}}}^{-1} A_1 {W_{\mathrm{s}}}^{\times} V_{\mathrm{s}} + {T_{p-s}}^{-1} {W_{\mathrm{s}}}^{\times} A_2 W_{\mathrm{s}} \\ &+ {T_{\mathrm{p-s}}}^{-1} {W_{\mathrm{s}}}^{\times} (A_1 V_{\mathrm{s}} + A_2 W_{\mathrm{s}}) + F_{\mathrm{d}} \end{aligned} \tag{16}$$

where $F_{\mathrm{p}}^{\mathrm{th}} = [u_2, 0, 0]^{\mathrm{T}}$ and u_2 is the thrust control quantity. By expanding (16), we have

$$\begin{aligned} u_2 &= 2a_{15} s_{\theta_{\mathrm{r}}} {q_{\mathrm{s}}}^2 + r_{\mathrm{s}}[2a_{15} c_{\theta_{\mathrm{r}}} s_{\psi_{\mathrm{r}}} q_{\mathrm{s}} - 2a_{24} c_{\theta_{\mathrm{r}}} c_{\psi_{\mathrm{r}}} p_{\mathrm{s}} \\ &+ (m_{11} + m_{22})(c_{\theta_{\mathrm{r}}} s_{\psi_{\mathrm{r}}} u_{\mathrm{s}} - c_{\theta_{\mathrm{r}}} c_{\psi_{\mathrm{r}}} v_{\mathrm{s}})] + F_{\mathrm{dx}} \\ &+ p_{\mathrm{s}}[-(m_{22} + m_{33})(c_{\theta_{\mathrm{r}}} s_{\psi_{\mathrm{r}}} w_{\mathrm{s}} + s_{\theta_{\mathrm{r}}} v_{\mathrm{s}})] \\ &+ q_{\mathrm{s}}(m_{11} + m_{33})(c_{\theta_{\mathrm{r}}} c_{\psi_{\mathrm{r}}} w_{\mathrm{s}} + s_{\theta_{\mathrm{r}}} u_{\mathrm{s}}) \\ &- 2a_{24} s_{\theta_{\mathrm{r}}} {p_{\mathrm{s}}}^2 \end{aligned} \tag{17}$$

where $s_{\theta_{\mathrm{r}}} \equiv \sin\theta_{\mathrm{r}}$ and $c_{\theta_{\mathrm{r}}} \equiv \cos\theta_{\mathrm{r}}$; $m_{11}, m_{22}, m_{33}, a_{15}$, and a_{24} are components in the apparent mass matrix; F_{dx} denotes the first component of F_{d}.

Obviously, with the variable ff_{dx} being irrelevant terms, the relation between the angular velocity component and the thrust is given as:

$$r_{\mathrm{s}} = \frac{1}{C}(u_2 + ff_{\mathrm{dx}}) \tag{18}$$

where C satisfies

$$\begin{aligned} C &= 2a_{15} c_{\theta_{\mathrm{r}}} s_{\psi_{\mathrm{r}}} q_{\mathrm{s}} - 2a_{24} c_{\theta_{\mathrm{r}}} c_{\psi_{\mathrm{r}}} p_{\mathrm{s}} + (m_{11} + m_{22}) \\ &(c_{\theta_{\mathrm{r}}} s_{\psi_{\mathrm{r}}} u_{\mathrm{s}} - c_{\theta_{\mathrm{r}}} c_{\psi_{\mathrm{r}}} v_{\mathrm{s}}) \end{aligned} \tag{19}$$

Next, substituting (18) into (14), the coupling influence of longitudinal thrust on lateral yaw angular acceleration can be obtained with the variable f being irrelevant terms.

$$\ddot{\varphi} = \frac{1}{C} \times \left(\frac{2\cos 2\zeta \sin\theta}{\cos^2\theta} q_{\mathrm{s}} - \frac{\sin\zeta}{\cos\theta} p_{\mathrm{s}} \right) u_2 + f \tag{20}$$

and the coupling coefficient is

$$b_4 = \frac{1}{C} \times \left(\frac{2\cos 2\zeta \sin\theta}{\cos^2\theta} q_{\mathrm{s}} - \frac{\sin\zeta}{\cos\theta} p_{\mathrm{s}} \right) \tag{21}$$

Note that the coupling relationship between the thrust u_2 and the yaw angular acceleration $\ddot{\varphi}$ is required only, and $b_4 u_2$ can be regarded as the known disturbance and dynamic feedforward compensation in the ESO and compensated in the control law. Besides, no matter what f is, we can view it as the unknown characteristic, which can be estimated and canceled by the ESO and ADRC, so f is assumed to be irrelevant.

3.3 Coupling of lateral brake deflection on longitudinal acceleration

Next, we will deduce the coupling relation of lateral brake deflection on the longitudinal vertical velocity. The transformation of velocity between the parafoil coordinate and geodetic coordinate can be obtained by:

$$\begin{bmatrix} V_x \\ V_y \\ V_z \end{bmatrix} = T_{\mathrm{g-s}}^{\mathrm{T}} \begin{bmatrix} u_{\mathrm{s}} \\ v_{\mathrm{s}} \\ w_{\mathrm{s}} \end{bmatrix} \tag{22}$$

where V_x, V_y, V_z denote the velocity components of the powered parafoil in the geodetic coordinate and T_{g-s} denotes the transformation from the geodetic coordinate to parafoil body coordinate.

$$T_{\mathrm{g-s}} = \begin{bmatrix} c_\theta c_\varphi & c_\theta s_\varphi & -s_\theta \\ s_\zeta s_\theta c_\varphi - c_\zeta s_\varphi & s_\zeta s_\theta s_\varphi + c_\zeta c_\varphi & s_\zeta c_\theta \\ c_\zeta s_\theta c_\varphi + s_\zeta s_\varphi & c_\zeta s_\theta s_\varphi - s_\zeta c_\varphi & c_\zeta c_\theta \end{bmatrix} \tag{23}$$

Then, the vertical velocity can be obtained from (22):

$$\dot{H} = V_z = -u_{\mathrm{s}} s_\theta + v_{\mathrm{s}} s_\zeta c_\theta + w_{\mathrm{s}} c_\zeta c_\theta \tag{24}$$

By differentiating vertical velocity with respect to time, the vertical acceleration is obtained by combining (12).

$$\begin{aligned} \ddot{H} &= -\dot{u}_{\mathrm{s}} s_\theta + \dot{v}_{\mathrm{s}} s_\zeta c_\theta + \dot{w}_{\mathrm{s}} c_\zeta c_\theta + p_{\mathrm{s}}(v_{\mathrm{s}} c_\zeta c_\theta \\ &- w_{\mathrm{s}} s_\zeta c_\theta) - q_{\mathrm{s}}(u_{\mathrm{s}} c_\zeta c_\theta + w_{\mathrm{s}} c_\zeta^2 s_\theta + w_{\mathrm{s}} s_\zeta^2 s_\theta) \\ &+ r_{\mathrm{s}}(u_{\mathrm{s}} s_\zeta c_\theta + v_{\mathrm{s}} c_\zeta^2 s_\theta + v_{\mathrm{s}} s_\zeta^2 s_\theta) \end{aligned} \tag{25}$$

From (25), the relation between the angular velocity and brake deflection is required. Because the change of aerodynamic force is determined by the brake deflection, the aerodynamic force acting on the powered parafoil is obtained from (1) and (4).

$$\begin{aligned} {F_{\mathrm{s}}}^{\mathrm{aero}} &= A_1 {W_{\mathrm{s}}}^{\times} V_{\mathrm{s}} + {W_{\mathrm{s}}}^{\times} (A_1 V_{\mathrm{s}} + A_2 W_{\mathrm{s}}) \\ &+ {W_{\mathrm{s}}}^{\times} A_2 W_{\mathrm{s}} + T_{\mathrm{p-s}}(m_{\mathrm{p}} \dot{V}_{\mathrm{p}} + {W_{\mathrm{p}}}^{\times} m_{\mathrm{p}} V_{\mathrm{p}} \\ &- F_{\mathrm{p}}^{\mathrm{aero}} - F_{\mathrm{p}}^{\mathrm{G}} - F_{\mathrm{p}}^{\mathrm{th}}) - {F_{\mathrm{s}}}^{\mathrm{G}} \end{aligned} \tag{26}$$

With the variable f_{d} being irrelevant terms, the first component of aerodynamic force can be rewritten as:

$$F_{\mathrm{sx}}{}^{\mathrm{aero}} = q_{\mathrm{s}}(m_{11}w_{\mathrm{s}} + m_{33}w_{\mathrm{s}}) - r_{\mathrm{s}}(m_{11}v_{\mathrm{s}} + 2a_{24}p_{\mathrm{s}} + m_{22}v_{\mathrm{s}}) + f_{\mathrm{d}} \tag{27}$$

Segmentation method was used to calculate the aerodynamic forces acting on the canopy [4,15,29]. The canopy is divided into eight distributed segments geometrically along the span-wise direction, the lift coefficient of each segment from outside to inside in turn is multiplied by the factor 0.6, 1.0, 1.16, and 1.24. The aerodynamic force of the parafoil body can be obtained by summing the aerodynamic forces of the eight segments. Moreover, lateral control is produced by changing the length of steering lines connected to outboard side and rear of the canopy. Pulling down steering lines leads to complex changes in the shape and orientation of the lifting surface the downward bending of the trailing edge forms the brake deflection angle (lateral control quantity). Therefore, the total aerodynamic forces of the parafoil consist of the force of its body and the brake deflection, which can be expressed as:

$$F_{\mathrm{s}}^{\mathrm{aero}} = F_{\mathrm{b}}^{aero} + F_{\mathrm{lf}}^{\mathrm{aero}} + F_{\mathrm{rf}}^{\mathrm{aero}} \tag{28}$$

where the subscript b denotes the body of parafoil and lf and rf denote the left and right brake deflection, respectively.

According to the segmentation method, the lift and drag forces of each segment of parafoil body are given as:

$$F_{\mathrm{L}_i} = 0.5k_iC_{\mathrm{L}_i}\rho S_i\sqrt{u_i^2 + w_i^2}[\,w_i\ 0\ -u_i\,]^{\mathrm{T}} \tag{29}$$

$$F_{\mathrm{D}_i} = -0.5C_{\mathrm{D}_i}\rho S_i\sqrt{u_i^2 + v_i^2 + w_i^2}[\,u_i\ v_i\ w_i\,]^{\mathrm{T}} \tag{30}$$

where k_i denotes the product factor; F_{L} and F_{D} denote the lift and drag forces, respectively; ρ denotes the density of air; S_i denotes the area of each segment; $V = (u_i, v_i, w_i)$ denotes the velocity of each segment in its own coordinate. The total aerodynamic force of the eight segments is represented as:

$$F_{\mathrm{b}}^{\mathrm{aero}} = \sum_{i=1}^{8} T_{i-O_{\mathrm{s}}}\left(F_{\mathrm{L}_i} + F_{\mathrm{D}_i}\right) \tag{31}$$

where $T_{i-O_{\mathrm{s}}}$ denotes the transformation from the local coordinate of the ith segment of the canopy to the parafoil coordinate. Since the variation of lift and drag coefficients is determined by the brake deflection and angle of attack, the lift and drag coefficients of each segment are given as:

$$C_{\mathrm{L}_i} = C_{L\alpha}(\alpha_i - \alpha_0) + j\sin^2(\alpha_i - \alpha_0)\cos(\alpha_i - \alpha_0) \tag{32}$$

$$C_{\mathrm{D}_i} = C_{D0} + \frac{C_{L\alpha}{}^2(\alpha_i - \alpha_0)^2(1+\delta)}{\pi\,\mathrm{AR}} + j\sin^3(\alpha_i - \alpha_0) \tag{33}$$

where $C_{L\alpha}$ is the line slope of lift; α_0 is the zero lift angle; C_{D0} is the profile drag; the subscript $i (i = 1, 2, \ldots, 8)$ denotes the ith segment of the canopy; α denotes the attack of angle; AR denotes the aspect ratio; j denotes a function of aspect ratio and the shape of the wing's lateral edges. Hoerner and Borst [30] proposed a calculation method of this parameter, as $1 < \mathrm{AR} < 2.5$, $\mathrm{j} = 3.33 - 1.33 \times \mathrm{AR}$; as $\mathrm{AR} \geq 2.5$, $j = 0$. δ is a small factor to allow for nonelliptic loading.

Because the additional aerodynamic force caused by brake deflection is also considered, so the attack of angles due to left and right brake deflection is:

$$\alpha_{\mathrm{lf}} = u_{\mathrm{l}} + \beta_{l,bf} - \phi, \alpha_{\mathrm{rf}} = u_{\mathrm{r}} + \beta_{r,bf} - \phi \tag{34}$$

where u_{l} and u_{r} denote the left and right brake deflection angle, respectively; $\beta_{l,bf}$, $\beta_{r,bf}$ denote the attack of angle between the airflow coordinate and parafoil coordinate, respectively; ϕ denotes the rigging angle. The lift and drag coefficients are calculated according to (32) and (33); then, the lift and drag forces due to brake deflection are:

$$F_{\mathrm{Lf}} = 0.5k_{\mathrm{bf}}C_{L,bf}\rho S_{\mathrm{bf}}\sqrt{u_{\mathrm{bf}}^2 + w_{\mathrm{bf}}^2}[\,w_{\mathrm{bf}}\ 0\ -u_{\mathrm{bf}}\,]^{\mathrm{T}} \tag{35}$$

$$F_{\mathrm{Df}} = -0.5C_{D,bf}\rho S_{\mathrm{bf}}\sqrt{u_{\mathrm{bf}}^2 + v_{\mathrm{bf}}^2 + w_{\mathrm{bf}}^2}[\,u_{\mathrm{bf}}\ v_{\mathrm{bf}}\ w_{\mathrm{bf}}\,]^{\mathrm{T}} \tag{36}$$

where the subscript bf denotes the left or right brake deflection and k_{bf} denotes the product factor; from (28) to (36), the first component of total aerodynamic force can be represented as:

$$F_{\mathrm{sx}}^{\mathrm{aero}} = Eu_{\mathrm{l}} + Fu_{\mathrm{r}} + f(u_{\mathrm{s}}, v_{\mathrm{s}}, w_{\mathrm{s}}, p_{\mathrm{s}}, q_{\mathrm{s}}, r_{\mathrm{s}}) \tag{37}$$

where E and F are the mathematical expressions obtained by (28)–(36). Combining (27) and (37) yields the relation between the brake deflection and angular velocity:

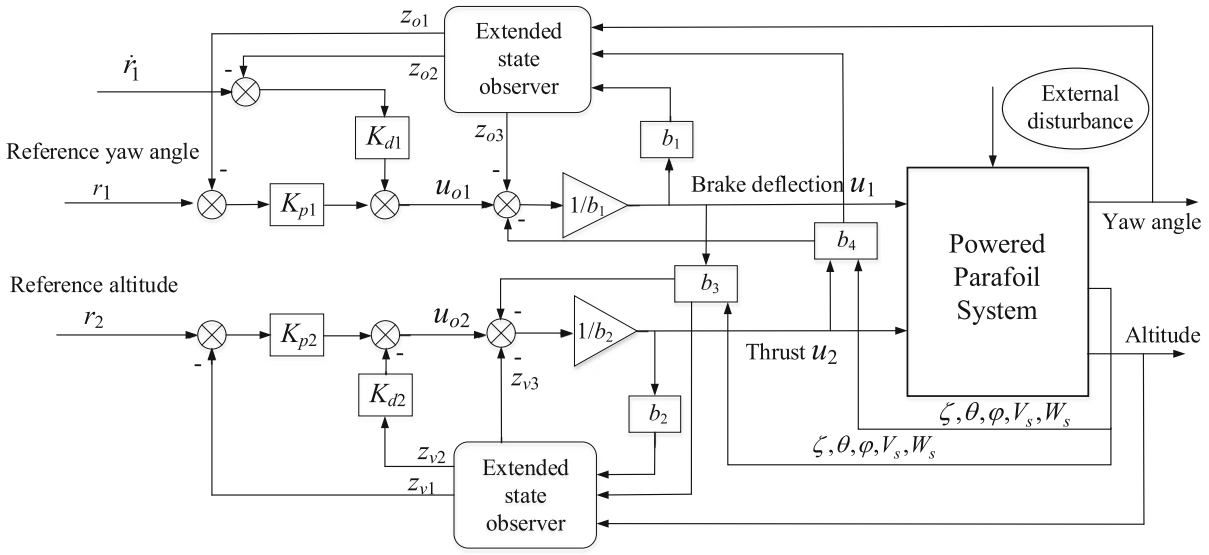

Fig. 3 Block diagram of double closed-loop decouple controller

$$q_{\mathrm{s}} = \frac{Eu_1 + Fu_{\mathrm{r}} + f + r_{\mathrm{s}}(m_{11}v_{\mathrm{s}} + 2a_{24}p_{\mathrm{s}} + m_{22}v_{\mathrm{s}}) - f_{\mathrm{d}}}{m_{11}w_{\mathrm{s}} + m_{33}w_{\mathrm{s}}} \tag{38}$$

Substituting (38) into (25), the longitudinal acceleration can be obtained by:

$$\begin{aligned}\ddot{H} = {} & \frac{\left(-u_{\mathrm{s}}c_{\zeta}\mathrm{c}_{\theta} - w_{\mathrm{s}}c_{\zeta}{}^{2}\mathrm{s}_{\theta} - w_{\mathrm{s}}s_{\zeta}{}^{2}s_{\theta}\right)}{(m_{11}+m_{33})w_{\mathrm{s}}}(Eu_1 + Fu_{\mathrm{r}}) \\ & + f + r_{\mathrm{s}}\left(u_{\mathrm{s}}s_{\zeta}\mathrm{c}_{\theta} + v_{\mathrm{s}}s_{\zeta}{}^{2}s_{\theta} + v_{\mathrm{s}}c_{\zeta}{}^{2}s_{\theta}\right) \\ & + \dot{v}_{\mathrm{s}}\mathrm{s}_{\zeta}\mathrm{c}_{\theta} + \dot{w}_{\mathrm{s}}\mathrm{c}_{\zeta}\mathrm{c}_{\theta} + p_{\mathrm{s}}(v_{\mathrm{s}}c_{\zeta}\mathrm{c}_{\theta} - w_{\mathrm{s}}s_{\zeta}\mathrm{c}_{\theta}) \\ & - \dot{u}_{\mathrm{s}}\mathrm{s}_{\theta}\end{aligned} \tag{39}$$

Therefore, the coupling relation of lateral brake deflection on the longitudinal vertical acceleration is obtained. The coupling coefficient is:

$$b_3 = \begin{cases} \dfrac{\left(-u_{\mathrm{s}}c_{\zeta}\mathrm{c}_{\theta} - w_{\mathrm{s}}c_{\zeta}{}^{2}\mathrm{s}_{\theta} - w_{\mathrm{s}}s_{\zeta}{}^{2}s_{\theta}\right)}{(m_{11}+m_{33})w_{\mathrm{s}}}E, u_1 \\ \dfrac{\left(-u_{\mathrm{s}}c_{\zeta}\mathrm{c}_{\theta} - w_{\mathrm{s}}c_{\zeta}{}^{2}\mathrm{s}_{\theta} - w_{\mathrm{s}}s_{\zeta}{}^{2}s_{\theta}\right)}{(m_{11}+m_{33})w_{\mathrm{s}}}F, u_{\mathrm{r}} \end{cases} \tag{40}$$

where the first term represents the coupling coefficient of left brake deflection angle on the longitudinal acceleration and the second term is the coupling of right brake deflection. Therefore, the cross-couplings of the powered parafoil are solved. Next, a compound control approach combing the feedforward cross-coupling compensation and ADRC is proposed. Note that the other uncertainties, resulting from the nonlinearity of the powered parafoil system, can be estimated and compensated by real-time dynamic feedback in ADRC.

4 Decoupling trajectory tracking control combining ADRC and feedforward coupling compensation

In this section, a double closed-loop decoupling controller combing ADRC and feedforward coupling compensation is shown in Fig. 3. DADRC is designed in both the lateral and longitudinal loop.

4.1 Lateral trajectory tracking loop

In the lateral controller, the yaw angle is output, and the control input is the lateral brake deflection. And the lateral trajectory tracking controller is designed to eliminate the lateral tracking error of the powered parafoil. According to the 3D guidance law [31], the lateral tracking error can converge to zero when the yaw angle of the powered parafoil tracks the reference yaw angle. The model of the powered parafoil is considered as a second-order nonlinear system, namely,

$$\ddot{\varphi} = f_{11}(\cdot) + b_1(t)u_1(t) + b_4(t)u_2(t) \tag{41}$$

where φ denotes the yaw angle; the nonlinear characteristic of system and $w(t)$ is considered as the unknown disturbance f_{11}; $u_1(t)$ denotes the lateral brake deflection; $b_1(t)$ denotes the input gain, the range of value can be obtained from the model, and (41) can be rewritten as:

$$\ddot{\varphi} = f_{11}(\cdot) + b_1(t)u_1(t) - b_0u_1(t) + b_4(t)u_2(t) + b_0u_1(t) \tag{42}$$

where b_0 is the equivalent input gain, $b_0 \approx b_1$. $f_{11}(\cdot) + b_1(t)u_1(t) - b_0u_1(t)$ can be viewed as the total disturbance in the lateral controller, including the unknown nonlinear dynamics, external disturbance, and the input gain error, which can be estimated and canceled by ESO and ADRC. So b_0 is viewed as a constant in the simulation study. $b_4(t)$ denotes the coupling coefficient of longitudinal thrust $u_2(t)$ on the lateral yaw angular acceleration obtained from (21). In order to improve the capacity of resisting the coupling and disturbance of the powered parafoil system, b_4 is directly regarded as the dynamic feedforward value in the ESO and the control law in the control system. Due to the nonlinear characteristic of the powered parafoil system, it cannot obtain the accurate mathematical expressions, and the external disturbance $w(t)$ is also unknown. Therefore, the unknown disturbance f_{11} can be estimated and then canceled by using ADRC, thus transforming (42) into an integrator to be easily controlled. We choose to estimate f_{11} in real time via an observer instead of relying on its mathematical representation. To do so, we first convert (42) into the extended state space form:

$$\begin{cases} \dot{x}_1(t) = x_2(t) \\ \dot{x}_2(t) = (x_3(t) + b_4u_2(t)) + b_1(t)u_1(t) \\ \dot{x}_3(t) = h(t) \\ y(t) = x_1(t) \end{cases} \tag{43}$$

with $x_3(t) = f_{11}$ added as an augmented state. $x_1(t)$ denotes the yaw angle, $h(t)$ is the derivative of f_{11} and unknown. The reason for increasing the order of the plant is to make f_{11} a state variable such that a state observer can be used to estimate it based on above extended state space model. The coupling influence $b_4(t)u_2(t)$ is designed as the known disturbance in the ESO, and the unknown disturbance f_{11} can be estimated by ESO, so that the estimation ability will be improved by reducing the estimation burden. Therefore, the third-order ESO is constructed as follows by considering the coupling compensation.

$$\begin{cases} \dot{Z}_o(t) = AZ_o(t) + B_o(t)u(t) + L_o(y(t) - \hat{y}(t)) \\ \hat{y}(t) = CZ_o(t) \end{cases} \tag{44}$$

$$A = \begin{bmatrix} 0 & 1 & 0 \\ 0 & 0 & 1 \\ 0 & 0 & 0 \end{bmatrix}, B_o = \begin{bmatrix} 0 & 0 \\ b_1 & b_4 \\ 0 & 0 \end{bmatrix} \tag{45}$$

where $Z_o(t) = [z_{o1}(t)\ z_{o2}(t)\ z_{o3}(t)]^T$ denotes the estimated states; $C = \begin{bmatrix} 1 & 0 & 0 \end{bmatrix}$; $\hat{y}(t)$ is the observed output for $y(t)$; $L_o = \begin{bmatrix} l_1 & l_2 & l_3 \end{bmatrix}$ is the observer gain vector. Gao [32] and Xie et al. [33] placed both the observer poles at $-w_{o1}$, and $w_{o1} > 0$, or equivalently,

$$\lambda(s) = s^3 + l_1s^2 + l_2s + l_3 = (s + w_{o1})^3 \tag{46}$$

that is,

$$l_1 = 3w_{o1}, l_2 = 3{w_{o1}}^2, l_3 = {w_{o1}}^3 \tag{47}$$

This estimation of f_{11} is a drastic departure from the existing model-based design paradigm since the information of the physical process needed by the controller is obtained from the plant input–output data. With the extended state observer in the lateral loop properly designed, the improved control law of brake deflection considering the feedforward coupling compensation is designed as:

$$u_1(t) = \frac{u_{o1}(t) - (z_{o3}(t) + b_4(t)u_2(t))}{b_1} \tag{48}$$

Note that with a well-tuned ESO, the estimation error in $z_{o3}(t)$ can be ignored, so the compensated plant will become a integrator to be easily tuned as follows.

$$\ddot{y}(t) = (f_{11} - z_{o3}(t)) + u_{o1}(t) - b_4(t)u_2(t) + b_4(t)u_2(t) \approx u_{o1}(t) \tag{49}$$

where $u_{o1}(t)$ is the output of the state error feedback.

In this paper, a proportional differential controller is adopted as the state error feedback. Thus, $u_{o1}(t)$ is obtained using

$$u_{o1}(t) = K_{p1}(r_1(t) - z_{o1}(t)) + K_{d1}(\dot{r_1}(t) - (z_{o2}(t))) \tag{50}$$

where K_{p1} and $K_{d1} > 0$ are the coefficients of proportional differential controller and $r_1(t)$ is the desired yaw angle in the lateral loop.

4.2 Longitudinal altitude loop

The longitudinal altitude loop is to control the vertical altitude of the powered parafoil system. The design process is the same with that of the lateral loop. Thus, the designed model can be rewritten as:

$$\ddot{H} = f_{22}(\cdot) + b_3(t)u_1(t) + b_2(t)u_2(t) \tag{51}$$

where H denotes the altitude; the nonlinear characteristic of system and $w(t)$ are considered as the unknown disturbance f_{22}; $b_3(t)$ denotes the coupling coefficient of lateral brake deflection control $u_1(t)$ on the longitudinal acceleration obtained from (40); $u_2(t)$ denotes the thrust; $b_2(t)$ is the input gain calculated from the model. Next, the coupling relation $b_3(t)u_1(t)$ is designed as the known disturbance in ESO; therefore, the third-order linear ESO with the consideration of coupling compensation is constructed as follows.

$$\begin{cases} \dot{Z}_{\mathrm{v}}(t) = AZ_{\mathrm{v}}(t) + B_{\mathrm{v}}(t)u(t) + L_{\mathrm{v}}(y(t) - \hat{y}(t)) \\ \hat{y}(t) = CZ_{\mathrm{v}}(t) \end{cases} \tag{52}$$

$$B_{\mathrm{v}} = \begin{bmatrix} 0 & 0 \\ b_3 & b_2 \\ 0 & 0 \end{bmatrix} \tag{53}$$

where $Z_{\mathrm{v}}(t) = [\, z_{v1}(t)\ z_{v2}(t)\ z_{v3}(t)\,]^{\mathrm{T}}$ denotes the estimated states; $\hat{y}(t)$ is the observed output for $y(t)$; and $L_{\mathrm{v}} = [\, 3w_{o2}\ 3{w_{o2}}^2\ {w_{o2}}^3\,]^{\mathrm{T}}$ is the observer gain vector. The improved control law for the plant considering the coupling compensation is obtained by

$$u_2(t) = \frac{u_{o2}(t) - (z_{v3}(t) + b_3(t)u_1(t))}{b_2} \tag{54}$$

where $u_{o2}(t)$ is the output of the state error feedback.

$$u_{o2}(t) = K_{p2}(r_2(t) - z_{v1}(t)) - K_{d2}z_{v2}(t) \tag{55}$$

where K_{p2}, $K_{d2} > 0$ are the coefficients of proportional differential controller and $r_2(t)$ is the reference altitude. From above design method, under the feedforward consideration of coupling compensation, this complex powered parafoil system is constructed as two decoupled integrators which to be easily controlled, and the tracking precision and disturbance rejection capacity can be improved simultaneously by reducing the coupling influence.

Table 1 Basic parameters of the parafoil system

Parameter	Value/Unit
Span	10.5/m
Chord	3.1/m
Aspect ratio	3.4
Area of canopy	33.0/m^2
Length of lines	6.8/m
Mass of canopy	10/kg
Mass of payload	80/kg
Characteristic area of payload	0.6m^2
Thrust	0–400.0/N

5 Simulation analysis

5.1 Simulation setup and results

In order to evaluate the validity of the proposed DADRC, numerical simulations have been carried out by a certain type of powered parafoils with physical parameters listed in Table 1. Use MATLAB software to conduct simulations on the established dynamic model of powered parafoil, the proposed DADRC, classical ADRC, and PID controllers. The parameters of the controllers are shown in Table 2. The working conditions are set as follows: initial velocity $V_{\mathrm{s}} = (14.9, 0, 2.1)$ m/s; initial position of the powered parafoil is $(-300, -600, 2000)$ m; initial Euler angles $(\zeta, \theta, \varphi) = (0, 0, 0)$; initial angular velocity $W_{\mathrm{s}} = (0, 0, 0)$ rad/s.

In the actual flight environment, the average wind and gust have a severe impact on the flight performance of the parafoil system [29,34]. In this simulation, the transverse average wind with a speed of 5 m/s and direction along the y-axis is added at 50 s; NASA's classic gust model [34] along the x-axis is added into the simulation environment at 100 s, which the velocity is set to 3m/s, the duration is 15 s; the reference trajectory is a circle around the origin O with a radius of 200 m; and the reference altitude is 1950 m; simulation time

Table 2 Parameters of controllers

DADRC, ADRC	PID
$w_{o1} = 2.7$	$k_{p1} = 11$
$w_{o2} = 3$	$k_{d1} = 20$
$K_{p1} = 0.04$	$k_{i1} = 0.4$
$K_{p2} = 0.0124$	$k_{p2} = 12$
$K_{d1} = 1.75$	$k_{d2} = 30$
$K_{d2} = 0.3$	$k_{i2} = 0.05$
$b_1 = 0.062$	
$b_2 = 0.01$	

and step are 250 and 0.025 s, respectively. Simulation results with DADRC, ADRC, PID are shown in Fig. 4.

Figure 4a and b show the controlled trajectories in the horizontal and vertical plane. It can be observed that DADRC reveals more stable performance with a smoother trajectory and a smaller tracking error than ADRC and PID, which indicates the high capacity of disturbance rejection of DADRC. Figure 4c indicates the comparison of the control quantities with the DADRC and ADRC, PID. It is obvious that the brake deflection of DADRC oscillates slighter than ADRC and PID for the coupling compensation, especially under the wind disturbance. The third figure in Fig. 4c shows an enlarged view for the longitudinal thrust after 50s when the wind comes. The longitudinal thrust of DADRC fluctuates less than ADRC and PID. At 68.28 s, the thrust of DADRC is 258.1 N, the thrust of ADRC is 265.7 N, and the thrust of PID is 310.3 N. Hence, DADRC is more energy saving than classical ADRC and PID under the wind disturbance. The estimated disturbance of the lateral and longitudinal controller is shown in Fig. 4d. The estimation of disturbance f_{11}, f_{22} in DADRC fluctuates slightly due to the coupling compensation, the fluctuations in the transient process caused by wind disturbance are effectively suppressed by reducing the estimation burden and time delay of ESO, and the estimated f_{11} and f_{22} can be canceled through the control law, making

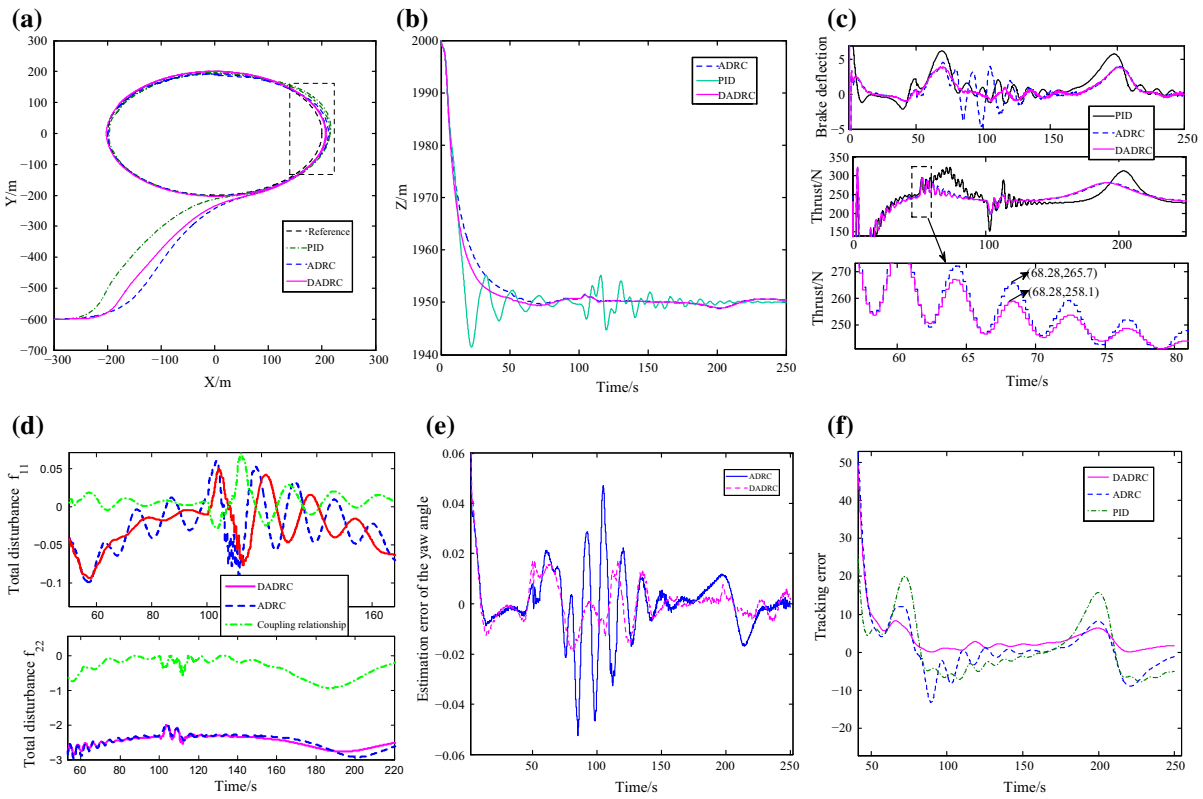

Fig. 4 Simulation results. **a** Trajectories in the horizontal plane, **b** trajectories in the vertical plane, **c** control quantities, **d** estimated disturbance of lateral and longitudinal controller, **e** estimation error and **f** tracking error

DADRC tolerant to the uncertainties. Figure 4e and f show the estimation error and tracking error. The average tracking error of DADRC achieves 2.41 m; the average tracking error of ADRC and PID is 4.19 and 5.46 m, respectively. Therefore, the control performance of the DADRC is better than the ADRC and PID.

5.2 Robustness performance

Guaranteeing robustness has long been an important objective of control system. In order to verify the robustness of the nonlinear system with DADRC, we introduce the Monte Carlo (MC) simulation technique [35,36] in this paper, and the 5 m/s mean wind along the y-axis and 3 m/s NASA gust along the x-axis are used to simulate the external disturbance. Moreover, the model uncertainties are also considered. It is assumed that the basic parameters of the model, involving area of canopy, length of lines, and mass of canopy, vary uniformly within $\pm 10\%$ of their nominal values; the air density and lift and drag coefficients vary uniformly within $\pm\,20\%$ of their nominal values to represent flight condition variations. Furthermore, the apparent mass has a strong effect on the flight dynamics of lightly loaded flight vehicles such as parafoils [37]. Hence, the perturbations of the apparent mass within $\pm\,20\%$ should also be taken into account. These uncertainties were categorized for this analysis using a uniform distribution. In addition, ITAE (integral time absolute error) index is introduced to evaluate the rapidness and accuracy of the system response, which can be represented as:

$$\mathrm{ITAE} = \int_0^T t\,|e(t)|\,\mathrm{d}t \tag{56}$$

where $e(t)$ is tracking error of the control system.

The MC simulation results with 200 sets of stochastic parameters are investigated under the consideration of adjusting time, overshoot, and ITAE index. A MC comparison results of DADRC with classical ADRC are shown in Fig. 5. The three axes are the adjusting time ts, overshoot $\sigma\,\%$, and ITAE. Robustness performance of perturbation system is shown in Table 3. It is generally known that the smaller the value of ITAE is, the better the control performance is; the more dense the MC simulation results are, the better the robustness of the system has. From Fig. 5 and Table 3, it can be

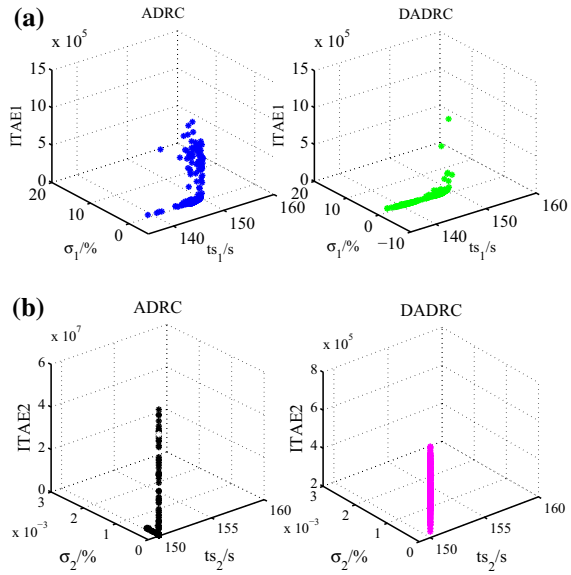

Fig. 5 MC comparison results of DADRC with ADRC of perturbation system. **a** Lateral loop and **b** longitudinal loop

observed that the dispersion of the lateral and longitudinal tracking error of DADRC is smaller than ADRC; therefore, the robustness of this proposed DADRC is stronger than classical ADRC.

6 Experimental analysis

6.1 Experimental setup

To further investigate the effectiveness of the proposed DADRC, the designed DADRC will be applied to the integrated experimental bench of the powered parafoil system. The semi-physical experiment platform is constructed to the greatest extent simulate the actual flight conditions for the powered parafoil system. The control algorithm is implemented in the embedded processor. The rig for the experiment is shown in Figs. 6 and 7. In the MCU, an ARM microprocessor (STM32F407GT6) is applied as the core control chip. With the help of the motor driving module (ESCON 36/3EC 414533), the motor is controlled by the MCU, and the optical-electricity encoder (DSP3806-16 $*$ 1024) was applied to the feedback of the turned position of motor. The thrust motor (GS C6362) was equipped on the back of the payload. The discrete values of the position and control input are gathered with the sample frequency of 4 Hz from the MCU via the serial communication. Fig-

Table 3 Robustness performance of perturbation system

Lateral	ts_1/s	$\sigma_1/\%$	ITAE1
ADRC	138.9 – 149.1	2.4 – 5.1	$1.08 - 1.1\times10^6$
DADRC	137.3 – 145.2	1.3 – 4.2	$0.35 - 1\times10^6$
Longitudinal	ts_2/s	$\sigma_2/\%$	ITAE2
ADRC	144.3 – 152.6	$0 - 4\times10^{-4}$	$0.08 - 6\times10^6$
DADRC	142.3 – 151.2	$0 - 1\times10^{-4}$	$0.06 - 7\times10^5$

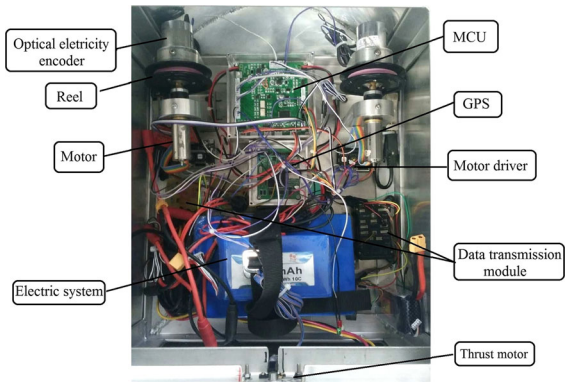

Fig. 6 Rudder and control system

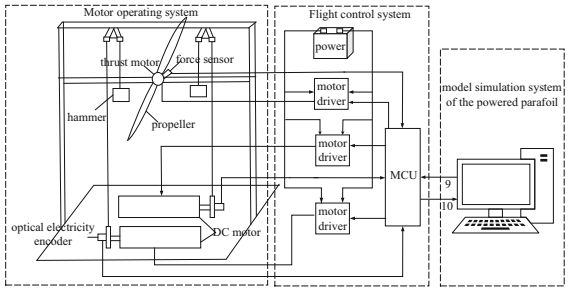

Fig. 7 Structure of experiment platform

ure 6 indicates the rudder of powered parafoil and control system. Figure 7 shows the structure of experiment platform, where the DC motor is used to manipulate the suspension lines on the trailing edge; the hammer is used to simulate the force in the process of pulling lines; the thrust motor is to manipulate the propeller.

In this experiment, the sampling frequency of GPS is 4 Hz; initial velocity and Euler angle and angular velocity are same with the simulation; initial position of the powered parafoil is (0, 0, 2000)m; the wind disturbance is similar with the simulation; the sampling period of ESO and control period are 0.25 s; the experiment duration is 250 s; the reference trajectory is a circle around

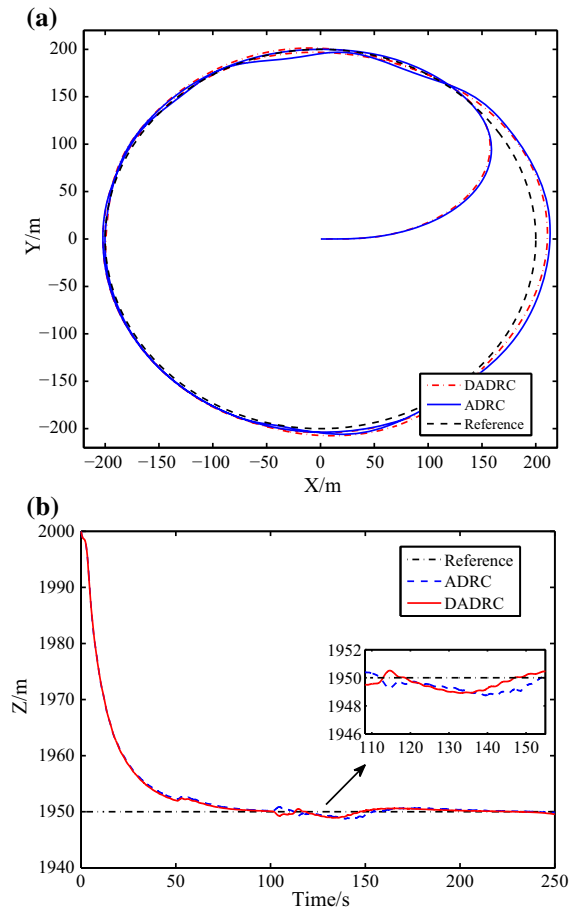

Fig. 8 Horizontal and vertical trajectories. **a** Trajectory in the horizontal plane and **b** trajectory in the vertical plane

the origin O with a radius of 200 m, the reference altitude is 1950 m. A comparison experimental results of DADRC and ADRC are shown in Figs. 8, 9 and 10.

6.2 Experimental results

Figure 8a and b show the controlled trajectories in the horizontal and vertical plane. From Fig. 8, DADRC

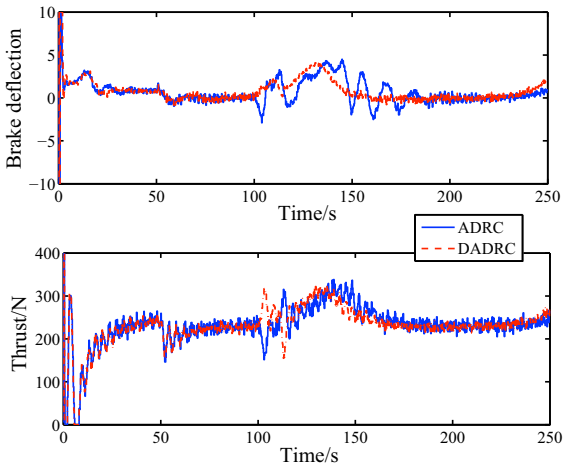

Fig. 9 Lateral brake deflection and longitudinal thrust

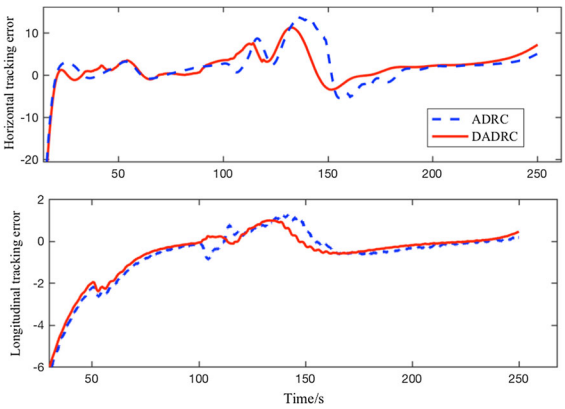

Fig. 10 Tracking error

has better tracking precision and the control effect. DADRC also has strong ability of disturbance rejection after the coupling compensation than ADRC. The maximum tracking errors in the lateral and longitudinal loop of DADRC are 8.5 and 1.1 m, respectively, while those of the classical ADRC controller are 12.3 and 1.7 m, respectively. Compared with the lateral controller, the longitudinal altitude controller of DADRC is slightly better than ADRC.

Figure 9 indicates the control quantities. As shown in Fig. 9, the lateral brake deflection of DADRC significantly outperforms the ADRC; when the wind comes, the response time is much shorter than ADRC, and the oscillation is smaller. It improves the capacity of the trajectory tracking and disturbance rejection largely. The tracking error of the lateral and longitudinal controller is shown in Fig. 10. With the help of the coupling compensation, DADRC effectively suppresses the wind disturbance and causes little tracking error of the horizontal distance. The mean absolute tracking error in the lateral and longitudinal loop of DADRC is 8.0364 and 3.1663 m, respectively, while that of the classical ADRC controller is 9.8861 and 3.9689 m, respectively, indicating that the proposed DADRC can not only suppress the disturbance effectively, but also improve the tracking precision of the system compared to classical ADRC.

7 Conclusion

In this paper, a novel decoupling controller of the powered parafoil system is proposed. The cross-coupling relations between the lateral and longitudinal motion are firstly analyzed and solved. Moreover, a decoupling trajectory tracking controller combining ADRC and feedforward coupling compensation is proposed, where the cross-couplings are designed as the known disturbance of ESO and directly compensated in the improved control law to reduce the coupling influence. Furthermore, under the cross-couplings compensation, this complex powered parafoil system is constructed as two ideal, decoupled integrators for the purpose of control design. The tracking precision and disturbance rejection capacity can be improved simultaneously. Mathematical simulations, robustness performance, and experimental results demonstrate that the proposed DADRC-based coupling compensation achieves better tracking performance and robustness against the uncertainties and internal and external disturbances compared with classical ADRC and PID.

Acknowledgements This work was supported by the National Natural Science Foundation of China under Grant Nos. 61273138, 61573197, and 61603051, the National Key Technology Research and Development Program of China under Grant (2015BAK06B04), the Research Fund of Tianjin Key Laboratory of Process Measurement and Control under Grant No. TKLPMC-201613.

Compliance with ethical standards

Conflict of interest The authors declare that they have no conflict of interest.

Human and animal rights This article does not contain any studies with human participants or animals performed by any of the authors.

Informed consent Informed consent was obtained from all individual participants included in the study.

Appendix

Stability analysis

Herein, it is necessary to show that this proposed control approach can operate with a bounded tracking error. From (41) and (51), we have

$$\begin{cases} \ddot{\varphi} = f_1 + b_1 u_1 + b_4 u_2 + w_1 \\ \ddot{H} = f_2 + b_2 u_1 + b_3 u_2 + w_2 \end{cases} \tag{57}$$

For the sake of analysis, the system is reformulated. Let $y_1 = \varphi$, $y_2 = H$, so we have

$$\begin{cases} \ddot{y}_1 = f_{11} + b_1 u_1 + b_4 u_2 \\ \ddot{y}_2 = f_{22} + b_3 u_1 + b_2 u_2 \end{cases} \tag{58}$$

where f_{11} and f_{22} represent the combined effect of internal dynamics and external disturbances in the lateral and longitudinal loop, respectively. Assuming f_{11} and f_{22} are differentiable such that $h_1 = \dot{f}_{11}, h_2 = \dot{f}_{22}$, two third-order ESO combing coupling compensation for the lateral and longitudinal control loop can be designed from (44) and (52):

$$\begin{cases} \dot{z}_{11} = z_{12} + l_{11}(y - z_{11}) \\ \dot{z}_{12} = (z_{13} + b_4 u_2) + l_{12}(y - z_{11}) + b_1 u_1 \\ \dot{z}_{13} = l_{13}(y - z_{11}) \end{cases} \tag{59}$$

$$\begin{cases} \dot{z}_{21} = z_{22} + l_{21}(y - z_{21}) \\ \dot{z}_{22} = (z_{23} + b_3 u_1) + l_{22}(y - z_{21}) + b_2 u_2 \\ \dot{z}_{23} = l_{23}(y - z_{21}) \end{cases} \tag{60}$$

and the total control law considering coupling compensation can be given by:

$$\begin{cases} b_1 u_1 = k_{\mathrm{p}1}(r_1 - z_{11}) + k_{\mathrm{d}1}(\dot{r}_1 - z_{12}) - (z_{13} + b_4 u_2) \\ b_2 u_2 = k_{\mathrm{p}2}(r_2 - z_{21}) + k_{\mathrm{d}2}(\dot{r}_2 - z_{22}) - (z_{23} + b_3 u_1) \end{cases} \tag{61}$$

Substituting (61) into (58), the two decoupled closed-loop systems become

$$\begin{cases} \ddot{y}_1 = k_{\mathrm{p}1}(r_1 - z_{11}) + k_{\mathrm{d}1}(\dot{r}_1 - z_{12}) + (f_{11} - z_{13}) \\ \ddot{y}_2 = k_{\mathrm{p}2}(r_2 - z_{21}) + k_{\mathrm{d}2}(\dot{r}_2 - z_{22}) + (f_{22} - z_{23}) \end{cases} \tag{62}$$

Note that with a well-tuned ESO, the terms $(f_{11} - z_{13})$, $(f_{22} - z_{23})$ are negligible [32,33]. Owing to the fact that the variation of the uncertain function is caused by the system's energy, which should be limited in finite time, then we give a assumption: the derivative of disturbance h_{11}, h_{22} is bounded, so $|h| \leq \delta$, where δ is a positive constant. And this assumption is met for most physical processes. It has been proven in [38] that the estimation error of the ESO is bounded and its upper bound monotonously decreases with the increase in the observer width $w_{\mathrm{o}1}$, $w_{\mathrm{o}2}$. The closed-loop tracking error is defined as $e_{ij}(t) = r_i^{(j-1)}(t) - x_{ij}(t)$, $(i = 1, 2)$, $(j = 1, 2)$, where $i = 1$ represents the lateral loop; $i = 2$ is the longitudinal loop; j denotes the states. Then, the estimation error is set as $\eta_{ij}(t) = x_{ij}(t) - z_{ij}(t)$. From (61), we can obtain for each loop, then

$$u_i = \begin{cases} \frac{k_{\mathrm{p}1}(e_{i1} + \eta_{i1}) + k_{\mathrm{d}1}(e_{i2} + \eta_{i2}) - (x_{i3} - \eta_{i3}) - b_4 u_2}{b_i}, i = 1 \\ \frac{k_{\mathrm{p}2}(e_{i1} + \eta_{i1}) + k_{\mathrm{d}2}(e_{i2} + \eta_{i2}) - (x_{i3} - \eta_{i3}) - b_3 u_1}{b_i}, i = 2 \end{cases} \tag{63}$$

It follows that

$$\begin{cases} \dot{e}_{i1} = e_{i2} \\ \dot{e}_{i2} = -k_{\mathrm{p}1}(e_{i1} + \eta_{i1}) - k_{\mathrm{d}1}(e_{i2} + \eta_{i2}) - \eta_{i3} \\ \dot{e}_i(t) = A_{e,i} e_i(t) + B_{\eta,i} \eta_{ij}(t) \end{cases} \tag{64}$$

where

$$A_{e,i} = \begin{bmatrix} 0 & 1 \\ -k_{\mathrm{p}i} & -k_{\mathrm{d}i} \end{bmatrix}, B_{\eta,i} = \begin{bmatrix} 0 & 0 & 0 \\ -k_{\mathrm{p}i} & -k_{\mathrm{d}i} & -1 \end{bmatrix} \tag{65}$$

Solving (64), we have

$$e_i(t) = e^{A_{e,i} t} e_i(0) + \int_0^t e^{A_{e,i}(t-\tau)} B_{\eta,i} \eta_{ij}(\tau) \mathrm{d}\tau \tag{66}$$

As proven in [38], with the assumption of $|h_{jj}| \leq \delta$ and finite and a finite time T_1, there exists a positive constant σ such that $|\eta_{ij}(t)| \leq \sigma, \forall t \geq T_1 > 0$, $w_{\mathrm{o}1} > 0$, $w_{\mathrm{o}2} > 0$, furthermore, $\sigma = O((1)/(w_{\mathrm{o}i}{}^q))$ for some positive q. So, from (66) and the convergence of ESO, we conclude that

$$\begin{cases} \left[B_{\eta,i} \eta_{ij}(\tau)\right]_1 = 0 \\ \left|\left[B_{\eta,i} \eta_{ij}(\tau)\right]_2\right| \leq (1 + k_{\mathrm{p}1} + k_{\mathrm{d}1})\sigma = \gamma, t \geq T_1 \end{cases} \tag{67}$$

Let $\varphi(t) = \int_0^t e^{A_{e,i}(t-\tau)} B_{\eta,i} \eta_{ij}(\tau) \mathrm{d}\tau$. Define $\psi = [\,0\ \gamma\,]^{\mathrm{T}}$. It follows that

$$|\varphi_k(t)| \leq \left|\left(A_{e,i}{}^{-1}\psi\right)_k\right| + \left|\left(A_{e,i}{}^{-1}e^{A_{e,i}t}\psi\right)_k\right| \tag{68}$$

Since

$$A_{e,i}{}^{-1} = \begin{bmatrix} -\frac{k_{di}}{k_{pi}} & -\frac{1}{k_{pi}} \\ 1 & 0 \end{bmatrix} = \begin{bmatrix} -\frac{2}{w_{ci}} & -\frac{1}{w_{ci}{}^2} \\ 1 & 0 \end{bmatrix} \tag{69}$$

we have

$$\left|\left(A_{e,i}{}^{-1}\psi\right)_k\right| = \begin{cases} \frac{\gamma}{w_{ci}{}^2}, k = 1 \\ 0, k = 2 \end{cases} \tag{70}$$

Since $A_{e,i}$ is Hurwitz, there exists a finite time $T_2 > 0$ such that

$$\left|\left[e^{A_{e,i}t}\right]_{mn}\right| \leq \frac{1}{w_{ci}{}^3} \tag{71}$$

for all $t \geq T_2$. Let

$$e^{A_{e,i}t} = \begin{bmatrix} o_{11} & o_{12} \\ o_{21} & o_{22} \end{bmatrix} \tag{72}$$

It follows that

$$\left|\left[e^{A_{e,i}t}e_i(0)\right]_k\right| \leq \frac{|e_{i1}(0)| + |e_{i2}(0)|}{w_{ci}{}^3} \tag{73}$$

for all $t \geq T_2$, where $e_{i,\text{sum}} = |e_{i1}(0)| + |e_{i2}(0)|$. We have

$$\left|\left[e^{A_{e,i}t}\psi\right]_k\right| \leq \frac{\gamma}{w_{ci}{}^3} \tag{74}$$

for all $t \geq T_3$, and

$$\left|\left(A_{e,i}{}^{-1}e^{A_{e,i}t}\psi\right)_k\right| \leq \begin{cases} \frac{1+2w_c}{w_{ci}{}^2}\frac{\gamma}{w_{ci}{}^3}, k = 1 \\ \frac{\gamma}{w_{ci}{}^3}, k = 2 \end{cases} \tag{75}$$

for all $t \geq T_3$. From (68), (70) and (75), we obtain

$$|\varphi_k(t)| \leq \begin{cases} \frac{\gamma}{w_c{}^2} + \frac{1+2w_c}{w_c{}^2}\frac{\gamma}{w_c{}^3}, k = 1 \\ \frac{\gamma}{w_c{}^3}, k = 2 \end{cases} \tag{76}$$

for all $t \geq T_3$. From (66), one has

$$e_i(t) \leq \left|\left[e^{A_{e,i}t}e_i(0)\right]_k\right| + |\varphi_k(t)| \tag{77}$$

According to (73) and (76), we have

$$\begin{aligned} e_{ij}(t) &\leq \begin{cases} \frac{|e_{i1}(0)|+|e_{i2}(0)|}{w_{ci}{}^3} + \frac{(1+2w_{ci})\gamma}{w_{ci}{}^5} + \frac{\gamma}{w_{ci}{}^2}, j = 1 \\ \frac{|e_{i1}(0)|+|e_{i2}(0)|+\gamma}{w_{ci}{}^3}, j = 2 \end{cases} \\ &\leq \rho_j \end{aligned} \tag{78}$$

for all $t \geq T_3$, $i = 1, 2$. And

$$\rho_j = \max\left\{\begin{matrix} \frac{|e_{i1}(0)|+|e_{i2}(0)|}{w_{ci}{}^3} + \frac{(1+2w_{ci})\gamma}{w_{ci}{}^5} + \frac{\gamma}{w_{ci}{}^2}, \\ \frac{|e_{i1}(0)|+|e_{i2}(0)|+\gamma}{w_{ci}{}^3} \end{matrix}\right\} \tag{79}$$

Remark The above proof shows that, with the assumption of bounded h and finite T_3, there exists a positive constant ρ_j such that the tracking error of both closed loops is bounded, and their upper limit will decrease as observer and controller bandwidths increase.

References

1. Yakimenko, O.A.: Precision Aerial Delivery Systems: Modeling, Dynamics, and Control. American Institute of Aeronautics and Astronautics, Inc, Reston (2015)
2. Watanabe, M., Ochi, Y.: Modeling and simulation of nonlinear dynamics of a powered paraglider. In: AIAA Guidance, Navigation and Control Conference and Exhibit, pp. 18–21 (2008)
3. Tao, J., Sun, Q., Liang, W., Chen, Z., He, Y., Dehmer, M.: Computational fluid dynamics based dynamic modeling of parafoil system. Appl. Math. Model. **54**(Supplement C), 136–150 (2018)
4. Xiong, J.: Research on the dynamics and homing project of parafoil system. National University of Defense Technology (2005)
5. Rogers, J., Slegers, N.: Robust parafoil terminal guidance using massively parallel processing. J. Guidance Control Dyn. **36**(5), 1336–1345 (2013)
6. Ward, M., Costello, M., Slegers, N.: Specialized system identification for parafoil and payload systems. J. Guidance Control Dyn. **35**(2), 588–597 (2012)
7. Nie, S., Cao, Y., Wu, Z.: Numerical simulation of parafoil inflation via a Robin–Neumann transmission-based approach. Proc. Inst. Mech. Eng. Part G J. Aerosp. Eng. (2017). https://doi.org/10.1177/0954410016688925
8. Altmann, H.: Influence of wind on terminal guidance and landing precision of autonomous parafoil systems. In: AIAA Aerodynamic Decelerator Systems (ADS) Conference 2013 (2013)
9. Zhu, E., Sun, Q., Tan, P., Chen, Z., Kang, X., He, Y.: Modeling of powered parafoil based on kirchhoff motion equation. Nonlinear Dyn. **79**(1), 617–629 (2015)

10. Luders, B., Ellertson, A., How, J.P., Sugel, I.: Wind uncertainty modeling and robust trajectory planning for autonomous parafoils. J. Guidance Control Dyn. **39**(7), 1614–1630 (2016)
11. Slegers, N., Costello, M.: Model predictive control of a parafoil and payload system. J. Guidance Control Dyn. **28**, 816–821 (2005)
12. Aoustin, Y., Martynenko, Y.: Control algorithms of the longitude motion of the powered paraglider. In: ASME 2012 11th Biennial Conference on Engineering Systems Design and Analysis, pp. 775–784 (2012)
13. Ochi, Y., Kondo, H., Watanabe, M.: Linear dynamics and PID flight control of a powered paraglider. In: AIAA Guidance, Navigation, & Control Conference (2013)
14. Li, B., Yang, L., He, Y., Han, J.: Energy-based controller decoupling of powered parafoil unmanned aerial vehicle. In: 2016 IEEE International Conference on Cyber Technology in Automation, Control, and Intelligent Systems (CYBER), pp. 313–320 (2016)
15. Tao, J., Sun, Q., Tan, P., Chen, Z., He, Y.: Autonomous homing control of a powered parafoil with insufficient altitude. ISA Trans. **65**, 516–524 (2016)
16. Tao, J., Sun, Q., Tan, P., Chen, Z., He, Y.: Active disturbance rejection control (ADRC)-based autonomous homing control of powered parafoils. Nonlinear Dyn. **86**(3), 1461–1476 (2016)
17. Tao, J., Sun, Q., Sun, H., Chen, Z., Dehmer, M., Sun, M.: Dynamic modeling and trajectory tracking control of parafoil system in wind environments. IEEE/ASME Trans. Mech. **22**(6), 2736–2745 (2017)
18. Ali, S.A., Langlois, N.: Sliding mode control for diesel engine air path subject to matched and unmatched disturbances using extended state observer. Math. Probl. Eng. **2013**(9), 1–11 (2013)
19. Radke, A., Gao, Z.: A survey of state and disturbance observers for practitioners. In: American Control Conference, p. 6. IEEE (2006)
20. Gao, Z.: On the centrality of disturbance rejection in automatic control. ISA Trans. **53**(4), 850–857 (2014)
21. Zhang, Y., Fan, C., Zhao, F., Ai, Z., Gong, Z.: Parameter tuning of ADRC and its application based on CCCSA. Nonlinear Dyn. **76**(2), 1185–1194 (2014)
22. Zhu, E., Pang, J., Sun, N., Gao, H., Sun, Q., Chen, Z.: Airship horizontal trajectory tracking control based on active disturbance rejection control (ADRC). Nonlinear Dyn. **75**(4), 725–734 (2014)
23. Xia, Y., Pu, F., Li, S., Gao, Y.: Lateral path tracking control of autonomous land vehicle based on adrc and differential flatness. IEEE Trans. Ind. Electron. **63**(5), 3091–3099 (2016)
24. Li, J., Xia, Y., Qi, X., Gao, Z.: On the necessity, scheme, and basis of the linear-nonlinear switching in active disturbance rejection control. IEEE Trans. Ind. Electron. **2**, 1425–1435 (2017)
25. Aboudonia, A., El-Badawy, A., Rashad, R.: Active anti-disturbance control of a quadrotor unmanned aerial vehicle using the command-filtering backstepping approach. Nonlinear Dyn. **90**(1), 581–597 (2017)
26. Zhang, C., Yang, J., Li, S., Yang, N.: A generalized active disturbance rejection control method for nonlinear uncertain systems subject to additive disturbance. Nonlinear Dyn. **83**(4), 2361–2372 (2016)
27. Zheng, Z., Huang, Y., Xie, L., Zhu, B.: Adaptive trajectory tracking control of a fully actuated surface vessel with asymmetrically constrained input and output. IEEE Trans. Control Syst. Technol. **PP**(99), 1–9 (2017). https://doi.org/10.1109/TCST.2017.2728518
28. Zheng, Z., Sun, L., Xie, L.: Error-constrained los path following of a surface vessel with actuator saturation and faults. IEEE Trans. Syst. Man Cybern. Syst. **PP**(99), 1–12 (2017). https://doi.org/10.1109/TSMC.2017.2717850
29. Tao, J., Liang, W., Sun, Q.L., Tan, P.L., Luo, S.Z., Chen, Z.Q., He, Y.P.: Modeling and control of a powered parafoil in wind and rain environments. IEEE Trans. Aerosp. Electron. Syst. **53**(PP), 1–1 (2017)
30. Hoerner, S.F., Borst, H.V.: Fluid-dynamic lift: practical information on aerodynamic and hydrodynamic lift. NASA STI/Recon Tech. Rep. A **76**, 32167 (1975)
31. Breivik, M., Fossen, T.I.: Principles of guidance-based path following in 2d and 3d. In: 44th IEEE Conference on Decision and Control, 2005 and 2005 European Control Conference. CDC-ECC'05, pp. 627–634. IEEE (2005)
32. Gao, Z.: Scaling and bandwidth-parameterization based controller tuning. Proc. Am. Control Conf. **6**, 4989–4996 (2003)
33. Xie, H., Song, K., Yang, S., Tatsumi, J., Zheng, Q., Zhang, H., Gao, Z.: On decoupling control of the VGT-EGR system in diesel engines: a new framework. IEEE Trans. Control Syst. Technol. **24**(5), 1788–1796 (2016)
34. Adelfang, O., Smith, S.: Gust models for launch vehicle ascent. In: 36th AIAA Aerospace Sciences Meeting and Exhibit, 1 Dec 1998
35. Mavrotas, G., Pechak, O., Siskos, E., Doukas, H., Psarras, J.: Robustness analysis in multi-objective mathematical programming using monte carlo simulation. Eur. J. Oper. Res. **240**(1), 193–201 (2015)
36. Stengel, R.F., Ray, L.R.: Application of stochastic robustness to aircraft control systems. J. Guidance Control Dyn. **14**(6), 1251–1259 (1991)
37. Lissaman, P., Brown, G.: Apparent mass effects on parafoil dynamics. In: Aerospace Design Conference, p. 1236 (1993)
38. Zheng, Q., Dong, L., Lee, D.H., Gao, Z.: Active disturbance rejection control for mems gyroscopes. IEEE Trans. Control Syst. Technol. **17**(6), 1432–1438 (2009)